Journal of Colloid and Interface Science 582 (2021) 1128–1135

Contents lists available at ScienceDirect

Journal of Colloid and Interface Science

journal homepage: www.elsevier.com/locate/jcis

# Development of dispersible radioluminescent silicate nanoparticles through a sacrificial layer approach

Eric Zhang [a], Yuriy Bandera [b], Ashley Dickey [b], Isabell Foulger [c], Joseph W. Kolis [b], Stephen H. Foulger [a,c,*]

[a] Center for Optical Materials Science and Engineering Technologies, Department of Materials Science and Engineering, Clemson University, Clemson, SC 29634-0971, USA
[b] Center for Optical Materials Science and Engineering Technologies, Department of Chemistry, Clemson University, Clemson, SC 29634-0971, USA
[c] Center for Optical Materials Science and Engineering Technologies, Department of Bioengineering, Clemson University, Clemson, SC 29634-0971, USA

## GRAPHICAL ABSTRACT

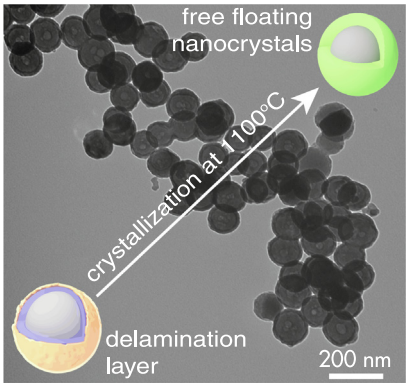


## ARTICLE INFO

*Article history:*
Received 6 April 2020
Revised 17 July 2020
Accepted 25 July 2020
Available online 10 August 2020

*Keywords:*
Core-shell
Radioluminescence
YPS:Ce
LPS:Ce

## ABSTRACT

X-rays offer low tissue attenuation with high penetration depth when used in medical applications and when coupled with radioluminescent nanoparticles, offer novel theranostic opportunities. In this role, the ideal scintillator requires a high degree of crystallinity for an application relevant radioluminescence, yet a key challenge is the irreversible aggregation of the particles at most crystallization temperatures. In this communication, a high temperature multi-composite reactor (HTMcR) process was successfully developed to recrystallize monodisperse scintillating particulates by employing a core-multishell architecture. The core–shell morphology of the particles consisted of a silica core over-coated with a rare earth (Re = $Y^{3+}$, $Lu^{3+}$, $Ce^{3+}$) oxide shell. This core–shell assembly was then encapsulated within a poly(divinylbenzene) shell which was converted to glassy carbon during the annealing & crystallization of the silica/rare earth oxide core–shell particle. This glassy carbon acted as a delamination layer and prevented the irreversible aggregation of the particles during the high temperature crystallization step. A subsequent low temperature annealing step in an air environment removed the glassy carbon and resulted in radioluminescent nanoparticles. Two monodisperse nanoparticle systems were synthesized using the HTMcR process including cerium doped $Y_2Si_2O_7$ and $Lu_2Si_2O_7$ with radioluminescence peaks at 427 and 399 nm, respectively. These particles may be employed as an *in vivo* light source for a noninvasive X-ray excited optogenetics.



## 1. Introduction

An attractive aspect of the use of X-rays in theranostic medical roles is the insignificant scattering of X-rays in tissue. This one

* Corresponding author at: Center for Optical Materials Science and Engineering Technologies, Department of Materials Science and Engineering, Clemson University, Clemson, SC 29634-0971, USA.
*E-mail address:* foulger@clemson.edu (S.H. Foulger).

https://doi.org/10.1016/j.jcis.2020.07.125
0021-9797/

feature has opened the possibility of deep tissue imaging with unrivaled spatial resolution and is the basis of X-rays many uses in the medical & biological community, including computed tomography, fluoroscopy, and radiotherapy [1–3]. Coupling these techniques with contrast agents in the form of scintillating materials has created new therapeutic and diagnostics tools, such as X-ray luminescence optical tomography (XLOT) and X-ray-excited optical luminescence (XEOL), as well as X-ray induced photodynamic therapy (X-PDT) [4–9]. Scintillation (or radioluminescent) materials emit visible photons when irradiated with X-rays and represent a form of optical down-conversion [10].

Radioluminescent materials are often composed of a host material doped with a lanthanide since elements in this series have a high atomic number which is favorable for X-ray absorption as well as electronic energy states which can emit across the UV, visible, and near-infrared region (NIR) of the electromagnetic spectrum [11,12]. An irradiated host matrix with a high atomic number element can generate high-energy electrons that can be down-converted in energy by a suitable choice of lanthanide sensitizers and emitters. Specific examples of these materials include the well known lutetium oxyorthosilicate doped with cerium ($Lu_2SiO_5$:Ce, LSO:Ce) [13,14], as well as the cerium doped yttrium and lutetium pyrosilicates, $Y_2Si_2O_7$:Ce (YPS:Ce) and $Lu_2Si_2O_7$:Ce (LPS:Ce), respectively.

Nanotechnology refers to cellular, molecular, and engineered materials which are distinguished by groups of atoms, molecules, and molecular fragments. These nanoscale objects with dimensions of approximately 100 nm can travel throughout the body where size-exclusion plays a role in their available sampling space [15]. The size-dependent permeability of the body can be exploited by material designers to create systems that can readily interact either on the exterior or interior of targeted biomolecules [16]. Radically new detection and treatment delivery systems have been developed over the last 35 years due to the access that these nanoscale devices have to specific regions within the body [17,18].

Optogenetics is a recently developed field of neuroscience that focuses on controlling the function of genetically-modified neurons with specific wavelengths of light [19]. This revolutionary technology utilizes genetically engineered cells which express a light-sensitive opsin, which is often an ion channel, G protein–coupled receptor, or pump. Conformational changes of these opsins with exposure to a specific wavelength of light leads to pump activation or channel opening, cell depolarization or hyperpolarization, and neural activation or silencing. Currently, light activation is predominantly achieved with fiber optic wave-guiding to the neurons, a relatively invasive procedure. An noninvasive technology, whereby excitation energy can be delivered to the neurons through tissue, is currently being explored with NIR absorbing up-converting nanoparticles [20] as well as Ce-doped $Gd_3(Al,Ga)_5O_{12}$ radioluminescent crystals [21]. In the latter effort, large millimeter sized crystals were embedded into mice to assess the *in vivo* scintillation-mediated actuation of neurons. The crossing of nanoparticles across the blood–brain barrier [22,23] suggests that opportunities exist in extending this latter approach with radioluminescent nanoparticles to achieve a fully noninvasive technology.

There have been a limited number of highly emissive non-hygroscopic and non-toxic radioluminescent particles presented in the literature, though the cerium doped lanthanide oxyorthosilicates and pyrosilicates are promising candidates [24–26]. One common challenge in synthesizing radioluminescent nanoparticles from rare earth silicates is the requirement of an annealing step at temperatures greater than 1000°C to achieve the reaction between the rare earth oxides and silica [27]. These elevated temperatures will normally result in the sintering of the particles together [28] and their irreversible aggregation, rendering them useless for biomedical applications [29].

The current effort presents the high temperature multi-composite reactor (HTMcR) process which is a general method for synthesizing radioluminescent nanoparticles from cerium doped lanthanide pyrosilicates, though other chemistries that require a high temperature annealing step may also benefit from the approach. The HTMcR process is demonstrated by synthesizing nanoparticles composed of cerium doped yttrium and lutetium pyrosilicates, YPS:Ce and LPS:Ce, respectively.

## 2. Results and discussion

Fig. 1i presents the general HTMcR process which can produce radioluminescent silicate particles doped with various rare earth (Re) species, while Fig. 1ii presents transmission electron microscope (TEM) images of the actual particles throughout the process. The procedure presented is general but was demonstrated with the rare earth species $Y^{3+}$, $Lu^{3+}$, and $Ce^{3+}$. Initially, a base catalyzed Stöber process was employed to synthesize uniform spherical silica particulates (122 ± 18 nm; cf. Fig. 1ii(a)) [30]. Silica is often employed as a passivation layer, a grafting agent platform, or a seed for core–shell synthesis [31,32], but in the HTMcR process, the silica core is repurposed as both a structural template and chemical platform for the final nanoparticle. To that end, a Re-hydrocarbonate ($Re(HCO_3)_3$) is next precipitated onto the silica core by a seed mediated growth technique [33]. The hydrocarbonate species on the silica cores were then oxidized at 750°C according to

$$2Re(HCO_3)_3 \overset{750^{\circ}C}{\rightarrow} Re_2O_3 + 3H_2O + CO_2 \quad (1)$$

to remove any water and/or carbon dioxide that may interfere with the HTMcR process, resulting in a $Re_2O_3$ shell on the particles (cf. Fig. 1ii(b)).

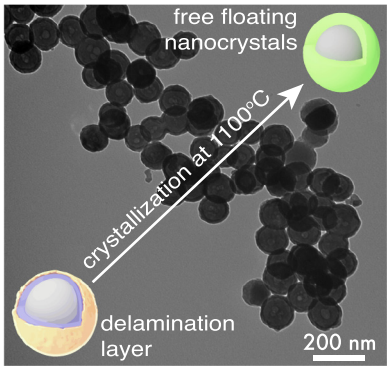


**Fig. 1. (i)** Scheme for the high temperature multi-composite reactor (HTMcR) process. Initially, a silica ($SiO_2$) core is over-coated with a rare earth oxide ($Re_2O_3$) shell. This $SiO_2/Re_2O_3$ core–shell particle is then surface modified with 3-(trimethoxysilyl) propyl methacrylate (MPS) to facilitate the attachment of an AIBN initiated polymerized DVB (pDVB) shell around the assembly before the $SiO_2/Re_2O_3$/pDVB particles undergo an 1000 °C annealing step in an inert atmosphere to convert the oxides to a radioluminescent rare earth pyrosilicate (RePS) phase. During the annealing step, the organic pDVB shell carbonizes to glassy carbon and frustrates particle to particle aggregation. After the RePS phase is formed, the temperature is reduced to 800 °C, a temperature where sintering is unlikely, and oxygen is introduced into the chamber to remove the glassy carbon. **(ii)** TEM images of core–shell particles during the various stages of the HTMcR process. **(a)** The initial $SiO_2$ cores (122 ± 18 nm) are **(b)** over-coated with yttrium hydrocarbonate doped with cerium ($SiO_2/Y(HCO)_3$:Ce) and oxidized at 750 °C for 30 min forming $SiO_2/Y_2O_3$:Ce particles (132 ± 21 nm). These latter particles are then **(c)** over-coated with pDVB after being surface modified with MPS, resulting in $SiO_2/Y_2O_3$:Ce/pDVB (162 ± 26 nm). **(d)** The $SiO_2/Y_2O_3$:Ce/pDVB particles were carbonized in a nitrogen environment for 36 h at 1100 °C to obtain $SiO_2$/YPS:Ce/$C_{glassy}$ (147 ± 19 nm). **(e)** Finally, the glassy carbon is removed by annealing at 800 °C in air to obtain $SiO_2$/YPS:Ce (127 ± 17). Particle sizing based on a population of 100 particles. Inserts are the particles size ($d_c$) diameter and the number of particles ($N(d_c)$).

To prevent aggregation at temperatures greater than 1000 °C that are needed to convert the oxide into a radioluminescent compound, a polymer coating is employed to encapsulate the inorganic core–shell particle. To accomplish this polymer overcoating, the $SiO_2/Re_2O_3$ surface of the particles were modified with 3-(trimethoxysilyl) propyl methacrylate (MPS), which introduces alkene functionality onto the particle's surface that facilitates the adherence of an *in situ* created polymer coating [34,35]. The MPS-modified particles were redispersed in acetonitrile solution containing the monomer divinylbenzene (DVB), and the free radical initiator azobisisobutyronitrile (AIBN) and underwent a precipitation polymerization to coat the particles. The polymerization of the bifunctional DVB around the particles, with the inclusion of the surface attached MPS [36], results in an adherent cross-linked pDVB coating on the particles (cf. Fig. 1ii(c)) [37–39]. These $SiO_2/Re_2O_3$/pDVB particles are then heated in an inert gas environment above 1000 °C to convert the pDVB into glassy carbon [40,41]. Simultaneously during the heating cycle to convert the pDVB to glassy carbon, the two oxides react with a silica core and form pyrosilicates (RePS) crystal:

$$Re_2O_3 + 2SiO_2 \overset{1000^{\circ}C}{\rightarrow} Re_2Si_2O_7. \quad (2)$$

In the final step, the temperature of the system is lowered to 800 °C and air is introduced into the chamber to remove the glassy carbon and generate unaggregated radioluminescent nanoparticles.

Specifically focusing on cerium doped yttrium pyrosilicate $Y_2Si_2O_7$:Ce (YPS:Ce) shell particles, the TEM image of the final $SiO_2$ particles with a YPS:Ce shell is presented in Fig. 3a. During the HTMcR process, on average, a 10.5 nm lanthanide hydrocarbonate shell grew on top of the silica size template (**S1**). After annealing at 750 °C for 30 min, the hydrocarbonate species oxidized and formed non-aggregated $SiO_2/Y_2O_3$:Ce particles with an average particle size of 132 ± 21 nm (cf. Fig. 1ii(b)). The decrease in particle size (ca. 11 nm) can be attributed to the loss of water, carbon dioxide, and densification. It was also observed that the lanthanide shell had a darker contrast in TEM images. This could be due to the heavier atomic elements reducing electron penetration through the particles. No difference in size was observed when the $SiO_2/Y_2O_3$:Ce particles were modified with MPS, however, the particles became hydrophobic due to the non-polar alkyl silane part in MPS molecule. pDVB was successfully polymerized onto the surface of $SiO_2/Y_2O_3$:Ce with a shell thickness of ca. 15 nm as seen by the triple contrast layer of the particles in Fig. 1ii(c). To form a YPS:Ce shell, during the conversion of the pDVB to glassy carbon, the reaction temperature was set to 1100 °CAfter annealing in an inert environment for 36 h, the particles ($SiO_2$/YPS:Ce/$C_{glassy}$) retained their spherical shape (cf. Fig. 1ii(d)) with an average particle size of 147 ± 19 nm (n = 100). There is a statistical significant 15 nm increase ($p < 0.01$) in the diameter (shell thickness ca. 7.5 nm) of the $SiO_2$/YPS:Ce/$C_{glassy}$ particles compared to their $SiO_2/Y_2O_3$:Ce precursor particles, indicating that the glassy carbon is present on the former particles.

The glassy carbon was removed at 800 °C by introducing air into the chamber, resulting in relatively monodisperse $SiO_2$/YPS:Ce (127 ± 17 nm) particles; Fig. 3a presents a TEM image of the particles after being annealed for 36 h at 1100 °C using the HTMcR process. Fig. 3b presents a field emission scanning electron microscope (FE-SEM) image of a set of final $SiO_2$/YPS:Ce particles that were annealed at 1100 °C for 24 h prior to removing the glassy carbon, while Fig. 3c presents particles that underwent the same procedure as the particles in Fig. 3b except no pDVB was used to coat the particles Fig. 13. The particles in Fig. 3b were not aggregated and exhibited a zeta potential of $\zeta = -47.8$ mV in deionized water, while the particles without the delamination layer afforded by the glassy carbon sintered into large micron sized slabs. A zeta potential with an absolute value greater than 30 mV is usually considered a signature of a stable colloidal system [42]. In contrast, the particles of Fig. 3c quickly settled to the bottom when dispersed in water Fig. 2.

As indicated earlier the particle size of $SiO_2/Y_2O_3$:Ce is 132 nm, on average the volume of the $Y_2O_3$:Ce shell encompasses 30% of the particles volume. After annealing the particulate through the HTMcR process, the final particle has a interior silica shell and

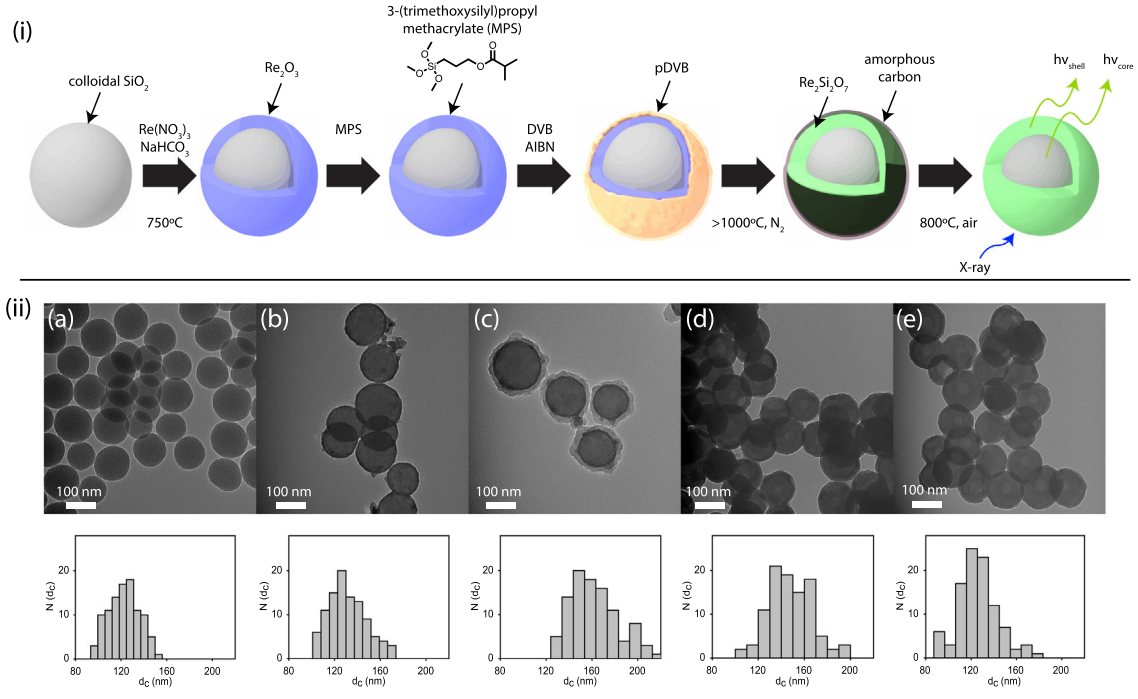


**Fig. 2.** **(a)** Different stages of the HTMcR particles dispersed in water and its respective counterpart particle without the sacrificial delamination layer.

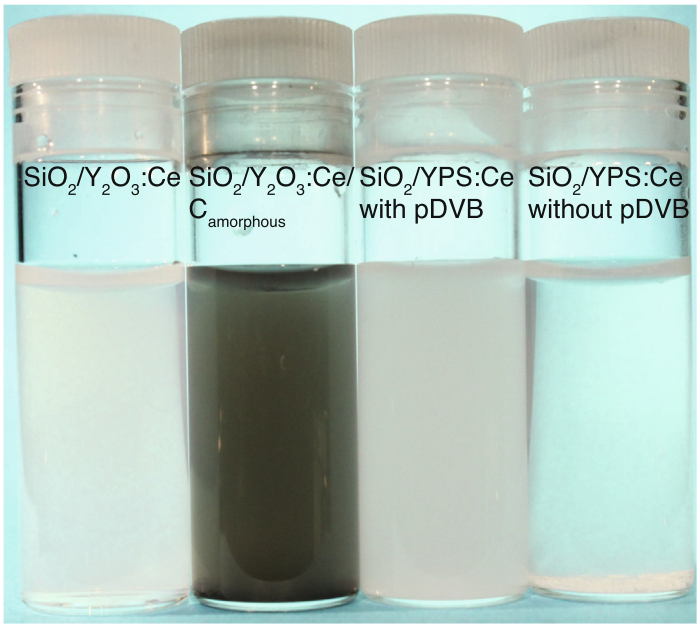


**Fig. 3.** **(a)** $SiO_2$/YPS:Ce particles annealed at 1100 °C for 36 h without any aggregation. **(b)** A non-sintered agglomerate of $SiO_2$/YPS:Ce particles synthesized by the HTMcR process and annealed for 24 h, while **(c)** the corresponding particles synthesized without pDVB and annealed at the same conditions sintered to micron sized particles.

YPS:Ce shell with a average particle size of 127 nm. The final $SiO_2$/YPS:Ce particle has a YPS:Ce shell that accounts for 55% of the particle's volume. The volume percent difference between the two stages of the particle's would imply that the YPS:Ce reached a densification of 87%. The overall volume shrinkage of the particle during the HTMcR process can be attributed to many factors such as densification of the silica core, recrystallization to the triclinic phase with a space group of $P\bar{1}$ (cf. Fig. 4), and loss of hydroxyls and gases in the pores of the particles In addition, all particulates exhibited the same space group when annealed at 1100 °C, with diminishing growth in crystallite size after two hours of annealing (cf. inset of Fig. 4).

The elemental distribution spectroscopy (EDS) of the $SiO_2$/YPS:Ce particles from scanning transmission electron microscopy in dark field indicated that cerium, due to its low concentration in the particles, appears to be uniformly distributed throughout the particle as indicated by the line scan of Fig. 5, while, as expected, the yttrium is concentrated in the shell of the particles [43,44]. The Y/Si and Ce/Y ratio in the final particles were 0.31 and 0.09, respectively (**S4**). This indicates that the rare earth species were fully incorporated onto the silica template since these ratios are similar to the element ratios employed in the synthetic process (0.30 and 0.08, respectively) and are within the 0.01% error of EDS.

The photoluminescence excitation (PLE) spectra of the dry $SiO_2$/YPS:Ce particles indicated three distinct peaks at 252 nm, 300 nm, and 341 nm when monitored at 400 nm (cf. Fig. 6a). The excitation peaks can be attributed to cerium's charge transfer and the transition from the $^4F_{7/2}$ and $^4F_{5/2}$ state to the 5d orbital [45]. A singular photoluminescence (PL) peak at 400 nm was observed when the particles were excited at 340 nm which can be attributed to the relaxation of electrons in the 5d orbital to its F states [46]. In order to compare the total light output of various nanoparticles, the integrated intensities of the PL spectrum were compared between $SiO_2$/YPS:Ce particles annealed at 1100 °C for different periods and is presented in Fig. 6b. Based on the maximum integrated PL, the particles that underwent a 24 h annealing period were optimal. Extending the annealing period past 24 h reduced the overall integrated luminescence and its hypothesized that a prolonged heating period may have (1) incorporated the glassy carbon into the particles creating unintentional defect sites that act as traps for radiative energy and/or (2) cerium oxidized from its active oxidation state ($Ce^{3+}$) to its non-emitting oxidation state ($Ce^{4+}$) [47]. Comparing the optically and X-ray excited emission of the particles indicates a slight red shift to ca. 427 nm with a low energy tail when the $SiO_2$/YPS:Ce particles are excited by X-rays (cf. Fig. 6a). This difference in the two luminescence spectra could be attributed to the architecture of the core–shell particles. Optical excitation energies can only penetrate the periphery of the particles and the resulting emission is localized to a volume within the shell, while the X-ray excitation has a deeper penetration depth. It is believed that this deep penetrating excitation energy would influence the overall X-ray luminescence spectra of core–shell nanoparticles. The silica core occupies 45% of the annealed nanoparticle's volume which was measured from the lighter contrast of the $SiO_2$/YPS:Ce TEM images. Correspondingly, the deep penetrating X-rays used as an excitation source may have excited both the YPS:Ce shell and the silica core, the latter having a X-ray luminescence peak at 450 nm [48]. This may have influenced the X-ray emission signature of the core–shell nanoparticle when compared to an optical excitation, resulting in a broad and red shifted X-ray luminescence.

The HTMcR process is a generalized methodology to produce scintillating non-aggregated nanoparticles and this versatility was demonstrated by synthesizing $SiO_2/Lu_2Si_2O_7$:Ce(LPS:Ce) nanoparticles in addition to the $SiO_2$/YPS:Ce particles. Fig. 7a presents $SiO_2$/LPS:Ce particles that were annealed at 1300 °C for 1 h. Similar to the $SiO_2$/YPS:Ce particles, the final $SiO_2$/LPS:Ce particles

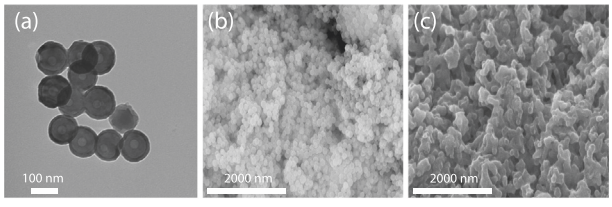


**Fig. 4.** Diffraction pattern of $SiO_2$/YPS:Ce particles annealed at 1100 °C compared to a lanthanide pyrosilicate single crystal (ICSD#171882). Inset is the calculated crystallite size of the different annealed $SiO_2$/YPS:Ce particles.

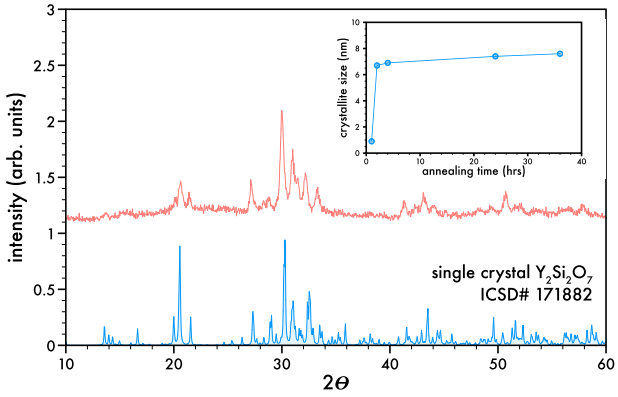


**Fig. 5.** Elemental distribution in $SiO_2$/YPS:Ce particles annealed at 1100 °C for 24 h. Scanning transmission electron microscope in dark field.

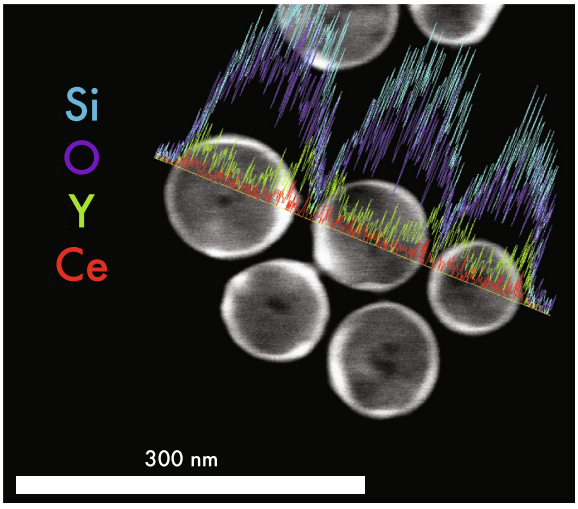


**Fig. 6.** **(a)** PLE ($\lambda_{emit}$ = 400 nm), PL ($\lambda_{excite}$ = 340 nm), and X-ray luminescence spectra of $SiO_2$/YPS:Ce particles. **(b)** Integrated PL intensities ($\lambda_{excite}$ = 340 nm) of the nanocrystal with annealing time at 1100 °C.

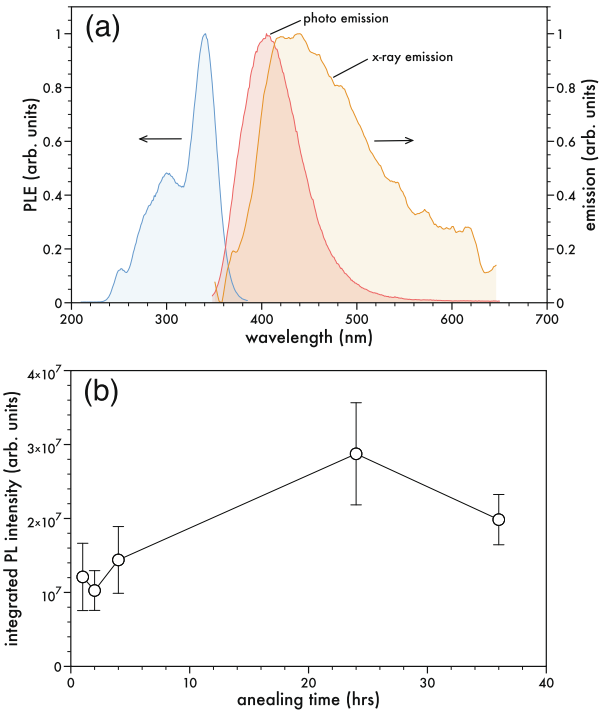


**Fig. 7.** **(a.)** $SiO_2$/LPS:Ce particles synthesized by the HTMcR process for 1 h at 1300 °C. **(b.)** Crystallization of $SiO_2$/LPS:Ce particles with a lattice spacing of 0.22 nm at higher magnification. **(c.)** Phase transformation of $SiO_2$/LPS:Ce particles from the triclinic $P\bar{1}$ to monoclinic $C2/m$ (ICSD#412249).

were non-aggregated spheres with a diameter of 123 ± 14 nm and exhibited crystallinity with lattice fringes of ca. 0.22 nm, indicated by Fig. 7b. X-ray diffraction spectra (cf. Fig. 7c) of the particles indicated a conversion from a mixture of $P\bar{1}$ and C2/m polymorphs to C2/m when the particles were annealed from 1100 °C to 1300 °C respectively.

The $SiO_2$/LPS:Ce nanoparticles synthesized by the HTMcR process have a X-ray emission spectrum with a peak at ca. 399 nm (cf. Fig. 8). Published X-ray and optically-excited emission spectra of bulk LPS:Ce crystals exhibit an asymmetric emission profile with a dominate peak at 380 nm [49]. In low temperature optically-excited emissions, this asymmetry is clearly due to two emission peaks at 380 nm and 415 nm, and is in agreement with the relaxation of the lowest 5d energy level to the $^2F_{5/2}$ and $^2F_{7/2}$ states, respectively [50]. The discrepancy between the X-ray emission of the $SiO_2$/LPS:Ce nanoparticles and its bulk counterpart is due to a greater probability of electrons relaxing from the lower 5d energy level to the $^2F_{7/2}$ state based on the peak emission wavelength (see Fig. 9).

Both the $SiO_2$/LPS:Ce and $SiO_2$/YPS:Ce nanoparticles have scintillating properties that originate from the inclusion of cerium. Despite the similar synthetic route for the two particles, the $SiO_2$/LPS:Ce X-ray emission is blue shifted relative to its counterpart $SiO_2$/YPS:Ce. This could be attributed to the greater X-ray absorption cross-section of the heavier atomic species lutetium where X-rays are primarily absorbed by the LPS:Ce shell [51] rather than the silica core, which has X-ray emission peak at ca. 450 nm [48]. The efficiency of LPS:Ce to absorb X-ray photons compared to YPS:Ce has been observed to increase light yield [52] and thus silica's dim radioluminescence is not observed for $SiO_2$/LPS:Ce synthesized using the HTMcR.

These scintillating particles may find use in a range of novel bio-related applications, such as optogenetics, where the light emission for opsin modulation can be achieved through radioluminescent nanoparticles [21] and the surface of the particles can be further modified with targeting moieties. To that end, cytotoxicity studies were performed on both the $SiO_2$/YPS:Ce and $SiO_2$/LPS:Ce particles in human embryonic kidney 293T cells (HEK-293T)(**S5**). For a 48 h incubation time, no change in cell growth relative to the control was observed with the $SiO_2$/YPS:Ce and $SiO_2$/LPS:Ce nanoparticles at concentrations up to $7.31 \times 10^5$ and $5.42 \times 10^5$ particles per HEK-293T cell, respectively. Previous cell viability studies on monodisperse 100 nm amorphous silica nanoparticles indicated a 50% reduction in EAHY926 cell viability ($TC_{50}$) when silica particles were dosed at ca. $1 \times 10^{12}$ particles per $cm^2$ of cell culture [53]. The maximum dosage of the $SiO_2$/YPS:Ce and $SiO_2$/LPS:Ce particles were approximately 15% and 11%, respectively, of this $TC_{50}$ value and indicated that the particles do not exhibit any profound toxicity to the HEK-293T cells over 48 h of incubation.

In summary, a high temperature multi-composite reactor (HTMcR) process was successfully developed to isolate and recrystallize nanoparticles at temperatures that would traditionally sinter these systems into large micron-sized monoliths. This was demonstrated with two different types of radioluminescent ca. 100 nm silicate nanoparticles that require temperatures over 1000 °C to crystallize. Control of the particle's optical and scintillating properties could be exerted through an annealing process which dictated both level and type of crystallinity. While the focus

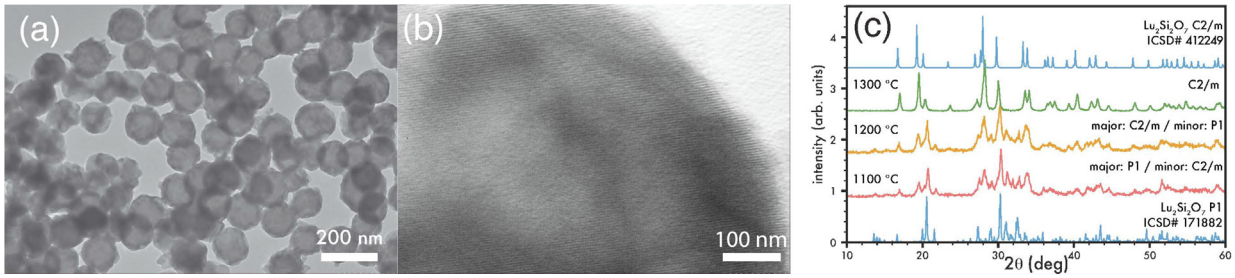


**Fig. 8.** Radioluminescence of $SiO_2$/LPS:Ce particles.

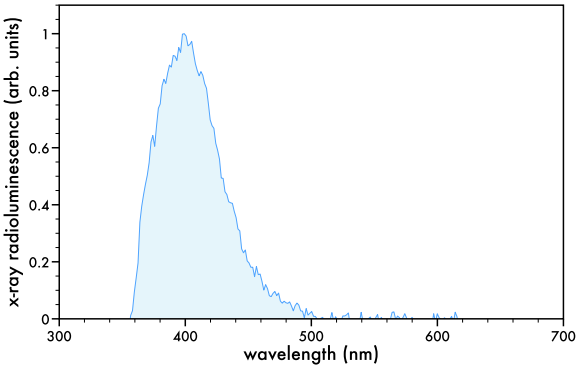


**Fig. 9.** (a) Silica synthesized by the Stöber process (122 ± 18 nm) and (b) deposition of $Y(HCO_3)_3$:Ce (143 ± 20 nm) on the silica size template.

of this communication was to demonstrate how the HTMcR process can create radioluminescent nanoparticles with a reduced aggregation, the technique developed here can explore different activators in new host lattices.

## CRediT authorship contribution statement

**Eric Zhang:** Conceptualization, Investigation, Writing - original draft. **Yuriy P. Bandera:** Investigation. **Ashley Dickey:** Investigation. **Isabell Foulger:** Investigation. **Joseph W. Kolis:** Conceptualization. **Stephen H. Foulger:** Funding acquisition, Conceptualization, Project administration.

## Declaration of Competing Interest

The authors declare that they have no known competing financial interests or personal relationships that could have appeared to influence the work reported in this paper.

## Acknowledgments

The authors thank John M. Ballato for his intellectual discussions on this topic. The authors thank Haijun Qian, Donald Mulwee and George Wetzel for their discussions on electron microscopy. The authors thank the National Institute of Standards and Technology (NIST) and Fachinformationszentrum Karlsruhe (FIZ) for their development in the inorganic crystal structure database (ICSD). The authors thank the Gregg-Graniteville Foundation and the National Science Foundation (OIA-1632881 & OIA-1655740) for financial support.

## Appendix A. Experimental

### *A.1. Materials and methods*

All reagents were purchased from Alfa Aesar, Sigma Aldrich, and Acros Organics. Tetraethyl orthosilicate (TEOS) and 3-(Trimethoxysilyl) propyl methacrylate (MPS) were distilled under vacuum. Divinyl benzene (DVB) was purified by passing through a basic alumina oxide filter to remove the inhibitor. AIBN was recrystallized from methanol. All other reagents were used without any purification.

### *A.2. Synthesis of silica core*

Silica particles were synthesized by a modified Stöber process with TEOS (67.18 mmol, 15.0 mL) dissolved in ethanol (150 mL), followed by addition of water (15.0 mL) and then an aqueous solution of $NH_4OH$ (29.38% v/v, 5.0 mL) was added dropwise. The reaction was stirred vigorously for 48 h. Silica was then separated and washed two times with water via centrifugation. A 95% yield of silica (3.8 g) was obtained by evaporation of aliquots in the suspension. The silica particles (122 nm) were dispersed in water (190 mL) for subsequent use.

### *A.3. Seed mediated growth of yttrium hydrocarbonate doped with cerium on silica*

The suspension of the silica spheres (16.64 mmol, 1.00 g) in water (500 mL) was stirred vigorously. Yttrium nitrate hexahydrate (5.48 mmol, 2.10 g) and cerium nitrate hexahydrate (0.44 mmol, 0.19 g) was then added to the reaction vessel. Sodium bicarbonate (16.67 mmol, 1.40 g) was dissolved in water (300 mL) and added dropwise into the main reaction vessel at a rate of 2.5 mL/min. After the sodium bicarbonate solution was fully incorporated, the reaction was stirred for an additional hour at room temperature. The $SiO_2/Y(HCO_3)_3$:Ce particulates was separated and washed two times with water via centrifugation. Once dried, the $SiO_2/Y(HCO_3)_3$:Ce particles was portioned for analytical characterization and further processing. A yield of 96% was obtained (2.52 g).

### *A.4. Oxidation of cerium doped yttrium hydrocarbonate shell*

The $SiO_2/Y(HCO_3)_3$:Ce particulates were oxidized to form $SiO_2/Y_2O_3$:Ce at 750 °C for 30 min, with a mass loss of 26.5%.

### *A.5. Modification of $SiO_2/Y_2O_3$:Ce particles with MPS*

The core–shell $SiO_2/Y_2O_3$:Ce particulates (1.20 g) was dispersed in 180 mL of a mixed solution of methanol and water (9:1, v/v) with MPS (1.01 mmol, 0.24 mL) and ammonia hydroxide

(1.68 mL). The reaction was mixed for 16 h at room temperature and then refluxed for 2 h under vigorous stirring conditions. The $SiO_2/Y_2O_3$:Ce/MPS particulates was washed two times in methanol via centrifugation.

### *A.6. Encapsulation of $SiO_2/Y_2O_3$:Ce particles with pDVB*

The $SiO_2/Y_2O_3$:Ce/MPS particulates (1.00 g) was dispersed in solution of acetonitrile (163 mL) with DVB (7.02 mmol, 1.00 mL) and AIBN (0.43 mmol, 0.07 g). The reaction vessel was degassed with $N_2$. Afterwards, the reaction vessel was heated to 55 °C for 20 h. The reaction was allowed to cool to room temperature and then washed two times with methanol via centrifugation.

### *A.7. High temperature annealing of $SiO_2/Y_2O_3$:Ce/pDVB*

Once dried, portions of the $SiO_2/Y_2O_3$:Ce/pDVB particles was transferred to a high temperature tube furnace, purged with nitrogen at a rate of 15 L/min for 20 min, and annealed at 1100 °C for varying time points. Afterwards, the black glassy carbon from $SiO_2$/YPS:Ce/$C_{glassy}$ particles was combusted at 800 °C with a constant flow of air at 15 L/min for 1 h. The final particulates obtain was $SiO_2$/YPS:Ce.

### *A.8. Encapsulating and thermal treatment of $SiO_2/Lu_2O_3$:Ce particles with pDVB*

The synthesis of $SiO_2$/LPS:Ce particulates followed the same process as the $SiO_2$/YPS:Ce particulates, with the exception of the annealing process where the $SiO_2/Lu_2O_3$:Ce/pDVB particulates was annealed at various temperatures.

### *A.9. Material characterization*

A Hitachi 4800 field emission scanning electron microscope was used for FE-SEM image acquisition, the particles were mounted onto a stub with double sided carbon tape followed by plasma coating with platinum for 1 min. A Hitachi 7600 TEM, Hitachi HT7830, and a Hitachi 2000 STEM was used to acquire TEM and EDS maps of the particulates, all samples were dispersed in methanol and drop casted onto a Formvar/Carbon 200 mesh TEM grid. RL of the different particulates were excited by a Amptek Mini-X tungsten source operating at 25 kV and 158 μA. RL measurements were taken in a free space environment where emitted light is directed from a 2 inch concave mirror to a MicroHT (Horiba Jobin Yvon) monochromator and a cooled synapse Horbia Jobin Yvon CCD detector with a grating of 300 mm and blaze of 500 nm. Samples were packed in a 6.5 mm × 1.5 mm round flat washer on a quartz slide. UV luminescence measurements were taken on a Jobin Yvon Fluorolog 3–222 spectrometer. The powder X-ray diffraction (pXRD) measurements were carried out on a Rigaku Ultima IV diffractometer using $Cu_{K\alpha}$ radiation ($\lambda$ = 1.5406 Å). The powder diffraction data was recorded in 0.02° increments over a $2\theta$ range of 5° to 65° at a scan speed of 1°/min. The crystallite size were calculated from the pXRD data using the Scherrer equation. Experimental pXRD patterns were compared to single crystal structures reported in the ICSD.

### *A.10. Cultured and MTS assay of human embryonic kidney (HEK) cells*

HEK-293T cells were obtained from American Type Culture Collection (CRL-3216) and were cultured in Dulbecco's modified eagle's media (DMEM) containing 50 mL of heat inactivated fetal bovine serum and 5 mL of glutamine in a 500 mL solution. Cells were cultured at 37 °C in a humidified atmosphere of 95% air/5% $CO_2$. The HEK cells were then plated in 96 well plates at a cell density of 4000 cells per well. After the cells were plated for 24 h, the cells were incubated with the different particulates ($SiO_2$/YPS:Ce and $SiO_2$/LPS:Ce). For $SiO_2$/YPS:Ce, the concentrations were $7.31 \times 10^3$, $7.31 \times 10^4$, and $7.31 \times 10^5$ particles per HEK cell. For $SiO_2$/LPS:Ce, the concentrations were $5.42 \times 10^3$, $5.42 \times 10^4$, and $5.42 \times 10^5$ particles per HEK cell. At each concentrations the cells were incubated for 24 and 48 h. At the end of each time point, the cell viability was measured using a [3-(4,5-dimethylthiazol-2-yl)-5-(3-carboxymethoxyphenyl)-2-(4-sulfophenyl)-2H-tetrazolium], inner salt (MTS) assay. The media was removed and the plates were washed several times with phosphate buffer solution before adding a solution containing 200 μL of DMEM media and 40 μL of MTS assay reagent. After 3 h the absorbance was measured using a plate reader at OD = 490 nm.

## Appendix B. Supplementary material

Supplementary data associated with this article can be found, in the online version, at https://doi.org/10.1016/j.jcis.2020.07.125.

## References

[1] A. Fouras, M.J. Kitchen, S. Dubsky, R.A. Lewis, S.B. Hooper, K. Hourigan, The past, present, and future of X-ray technology for in vivo imaging of function and form, J. Appl. Phys. 105 (10) (2009) 14.
[2] A. Bravin, P. Coan, P. Suortti, X-ray phase-contrast imaging: from pre-clinical applications towards clinics, Phys. Med. Biol. 58 (1) (2013) R1–R35.
[3] Q. Chen, J. Wu, X. Ou, B. Huang, J. Almutlaq, A.A. Zhumekenov, X. Guan, S. Han, L. Liang, Z. Yi, J. Li, X. Xie, Y. Wang, Y. Li, D. Fan, D.B.L. Teh, A.H. All, O.F. Mohammed, O.M. Bakr, T. Wu, M. Bettinelli, H. Yang, W. Huang, X. Liu, All-inorganic perovskite nanocrystal scintillators, Nature 561 (7721) (2018) 88–93.
[4] J. Della Rocca, D.M. Liu, W.B. Lin, Nanoscale metal-organic frameworks for biomedical imaging and drug delivery, Acc. Chem. Res. 44 (10) (2011) 957–968.
[5] H. Chen, T. Moore, B. Qi, D.C. Colvin, E.K. Jelen, D.A. Hitchock, J. He, T.O. Mefford, J.C. Gore, F. Alexis, J.N. Anker, Monitoring ph-triggered drug release from radioluminescent nanocapsules with x-ray excited optical luminescence, ACS nano 7 (2) (2013) 1178–1187.
[6] J. Xie, L. Gong, S. Zhu, Y. Yong, Z. Gu, Y. Zhao, Emerging strategies of nanomaterial-mediated tumor radiosensitization, Adv. Mater. 31 (3) (2019) 1802244.
[7] W. Fan, W. Tang, J. Lau, Z. Shen, J. Xie, J. Shi, X. Chen, Breaking the depth dependence by nanotechnology-enhanced x-ray-excited deep cancer theranostics, Adv. Mater. 31 (12) (2019) 1806381.
[8] W. Sun, T. Shi, L. Luo, X. Chen, P. Lv, Y. Lv, Y. Zhuang, J. Zhu, G. Liu, X. Chen, H. Chen, Monodisperse and uniform mesoporous silicate nanosensitizers achieve low-dose x-ray-induced deep-penetrating photodynamic therapy, Adv. Mater. 31 (16) (2019) 1808024.
[9] W. Sun, Z. Zhou, G. Pratx, X. Chen, H. Chen, Nanoscintillator-mediated x-ray induced photodynamic therapy for deep-seated tumors: From concept to biomedical applications, Theranostics 10 (3) (2020) 1296–1318.
[10] S.E. Derenzo, M.J. Weber, E. Bourret-Courchesne, M.K. Klintenberg, The quest for the ideal inorganic scintillator, Nucl. Instrum. Methods Phys. Res., Sect. A 505 (1–2) (2003) 111–117.
[11] J.J. Zhou, J.L. Leano, Z.Y. Liu, D.Y. Jin, K.L. Wong, R.S. Liu, J.C.G. Bunzli, Impact of lanthanide nanomaterials on photonic devices and smart applications, Small 14 (40) (2018) 29.
[12] Takayuki Yanagida, Study of rare-earth-doped scintillators, Opt. Mater. 35 (11) (2013) 1987–1992.
[13] C.L. Melcher, J.S. Schweitzer, Cerium-doped lutetium oxyorthosilicate - a fast, efficient new scintillator, IEEE Trans. Nucl. Sci. 39 (4) (1992) 502–505.
[14] C.L. Melcher, Scintillation crystals for pet, J. Nucl. Med. 41 (2000) 1051–1055.
[15] H. Gao, W. Shi, L.B. Freund, Mechanics of receptor-mediated endocytosis, Proc Natl Acad Sci U S A 102 (27) (2005) 9469–9474.
[16] M. Goldberg, R. Langer, X.Q. Jia, Nanostructured materials for applications in drug delivery and tissue engineering, J. Biomater. Sci.-Polym. Ed. 18 (3) (2007) 241–268.
[17] D. Kim, K. Shin, S.G. Kwon, T. Hyeon, Synthesis and biomedical applications of multifunctional nanoparticles, Adv. Mater. 30 (49) (2018) 1802309.
[18] J.J. Giner-Casare, M. Henriksen-Lacey, M. Coronado-Puchau, L.M. Liz-Marzan, Inorganic nanoparticles for biomedicine: where materials scientists meet medical research elsevier enhanced reader, Mater. Today 19 (1) (2016) 19–28.
[19] L. Fenno, O. Yizhar, K. Deisseroth, The Development and Application of Optogenetics, volume 34 of Annual Review of Neuroscience, pages 389–412. Annual Reviews, Palo Alto, 2011.

[20] Shuo Chen, Adam Z. Weitemier, Xiao Zeng, Linmeng He, Xiyu Wang, Yanqiu Tao, Arthur J.Y. Huang, Yuki Hashimotodani, Masanobu Kano, Hirohide Iwasaki, Laxmi Kumar Parajuli, Shigeo Okabe, Daniel B. Loong Teh, Angelo H. All, Iku Tsutsui-Kimura, Kenji F. Tanaka, Xiaogang Liu, Thomas J. McHugh, Near-infrared deep brain stimulation via upconversion nanoparticle-mediated optogenetics. Science, 359(6376), 679–683, 2018.
[21] T. Matsubara, T. Yanagida, N. Kawaguchi, T. Nakano, J. Yoshimoto, S.P. Tsunoda, S. Horigane, S. Ueda, S. Takemoto-Kimura, H. Kandori, A. Yamanaka, T. Yamashita, Remote control of neural function by x-ray-induced scintillation. bioRxiv, page 798790, 2019.
[22] M. Shilo, A. Sharon, K. Baranes, M. Motiei, J.P. Lellouche, R. Popovtzer, The effect of nanoparticle size on the probability to cross the blood-brain barrier: an in-vitro endothelial cell model, J. Nanobiotechnol. 13 (2015) 19.
[23] Y.H. Tsou, X.Q. Zhang, H. Zhu, S. Syed, X. Xu, Drug delivery to the brain across the blood-brain barrier using nanomaterials, Small 13 (43) (2017).
[24] Aundrea F. Bartley, Kavitha Abiraman, Luke T. Stewart, Mohammed Iqbal Hossain, David M. Gahan, Abhishek V. Kamath, Mary K. Burdette, Shaida Andrabe, Stephen H. Foulger, Lori L. McMahon, Lynn E. Dobrunz. Lso:ce inorganic scintillators are biocompatible with neuronal and circuit function. Frontiers in Synaptic Neuroscience, 11, 2019.
[25] Mary K. Burdette, Yuriy P. Bandera, Eric Zhang, Artem Trofimov, Ashley Dickey, Isabell Foulger, Joseph W. Kolis, Kelli E. Cannon, Aundrea F. Bartley, Lynn E. Dobrunz, Mark S. Bolding, Lori McMahon, Stephen H. Foulger, Organic fluorophore coated polycrystalline ceramic lso:ce scintillators for x-ray bioimaging, Langmuir 35 (1) (2019) 171–182.
[26] Shani Egodawatte, Eric Zhang, Tessa J. Posey, Grayson R. Gimblet, Stephen H. Foulger, Hans-Conrad zur Loye, Synthesis of scintillating ce3+-doped lu2si2o7 nanoparticles using the salt-supported high temperature (ssht) method: Solid state chemistry at the nanoscale, Acs Appl. Nano Mater. 2 (4) (2019) 1857–1865.
[27] Ziqi Sun, Yanchun Zhou, Meishuan Li, Low-temperature synthesis and sintering of γ-y2si2o7, J. Mater. Res. 21 (6) (2006) 1443–1450.
[28] F.B. Swinkels, M.F. Ashby, A second report on sintering diagrams, Acta Metall. 29 (2) (1981) 259–281.
[29] L.J. Cruz, M.A. Stammes, I. Que, E.R. van Beek, V.T. Knol-Blankevoort, T.J.A. Snoeks, A. Chan, E.L. Kaijzel, Cwgm Lowik, Effect of plga np size on efficiency to target traumatic brain injury, J. Control. Release 223 (2016) 31–41.
[30] W. Stober, A. Fink, Controlled growth of monodisperse silica spheres in the micron size range, J. Colloid Interface Sci 26 (1968) 62–69.
[31] S.H. Joo, J.Y. Park, C. Tsung, Y. Yamada, P. Yang, G. Somorjai, Thermally stable pt/mesoporous silica core-shell nanocatalysts for high temperature reactions, Nat. Mater. 8 (2009) 126–131.
[32] K. Ohno, T. Morinaga, K. Koh, Y. Tsujii, T. Fukuda, Synthesis of monodisperse silica particles coated with well-defined, high-density polymer brushes by surface-initiated atom transfer radical polymerization, Macromolecules 38 (2005) 2137–2142.
[33] H. Giesche, E. Matijevic, Preparation, characterization, and sinterability of well-defined silica/yttria powders, J. Mater. Res. 9 (02) (2011) 436–450.
[34] Sarita Kango, Susheel Kalia, Annamaria Celli, James Njuguna, Youssef Habibi, Rajesh Kumar, Surface modification of inorganic nanoparticles for development of organic–inorganic nanocomposites—a review, Prog. Polym. Sci. 38 (8) (2013) 1232–1261.
[35] Shadpour Mallakpour, Maryam Madani, A review of current coupling agents for modification of metal oxide nanoparticles, Prog. Org. Coat. 86 (2015) 194–207.
[36] G.L. Li, H. Mohwald, D.G. Shchukin, Precipitation polymerization for fabrication of complex core-shell hybrid particles and hollow structures, Chem. Soc. Rev. 42 (8) (2013) 3628–3646.
[37] Daniel Amara, Judith Grinblat, Shlomo Margel, Synthesis of magnetic iron and iron oxide micrometre-sized composite particles of narrow size distribution by annealing iron salts entrapped within uniform porous poly(divinylbenzene) microspheres, J. Mater. Chem. 20 (10) (2010) 1899.
[38] J.S. Downey, R.S. Frank, W. Li, D.H. Stover, Growth mechanism of poly (divinylbenzene) microspheres in precipitation polymerization, Macromolecules 32 (1999) 2838–2844.
[39] F. Caruso, Nanoengineering of particle surfaces, Adv. Mater. 13 (2001) 11–22.
[40] Huseyin Zengin, Gulay Zengin, Wensheng Zhou, Chris M. Topping, Dennis W. Smith, Stephen H. Foulger, Preparation and characterization of bis-ortho-diynylarene (boda)-derived submicrogratings, Polym. Eng. Sci. 47 (12) (2007) 2095–2099.
[41] H.V. Shah, S.T. Brittain, Q. Huang, S.J. Hwu, G.M. Whitesides, D.W. Smith, Bis-o-diynylarene (boda) derived polynaphthalenes as precursors to glassy carbon microstructures, Chem. Mater. 11 (10) (1999) 2623–2625.
[42] M.A. Daniele, M.L. Shaughnessy, R. Roeder, A. Childress, Y.P. Bandera, S. Foulger, Magnetic nanoclusters exhibiting protein-activated near-infrared fluorescence, ACSNano 7 (1) (2012) 203–213.
[43] Ahmet Faik Demirors, Alfons van Blaaderen, Arnout Imhof, Synthesis of eccentric titania-silica core-shell and composite particles, Chem. Mater. 21 (2009) 979–984.
[44] C.I. Zoldesi, A. Imhof, Synthesis of monodisperse colloidal spheres, capsules, and microballons, by emulsion templating, Adv. Mater. 17 (7) (2005) 924–928.
[45] L. Marciniak, D. Hreniak, A. Dobrowolska, E. Zych, Size-dependent luminescence in y2si2o7 nanoparticles doped with ce3+ ions, Appl. Phys. A 99 (4) (2010) 871–877.
[46] Yong Li, Xiantao Wei, Min Yin, Ye Tao, Energy transfer processes in ce3+ and tb3+ co-doped ln2si2o7 (ln=y, gd), Opt. Mater. 33 (8) (2011) 1239–1242.
[47] J. Lin, G. Yao, Y. Dong, B. Park, M. Su, Does ce 4+ play a role in the luminescence of lapo4:ce?, J. Alloy. Compd. 225 (1995) 124–128.
[48] M.J. Marrone, Radiation-induced luminescence in silica core optical fibers, Appl. Phys. Lett. 38 (3) (1981) 115–117.
[49] Q. Wei, J. Zhuang, G. Liu, Z. Zhou, H. Yang, J. Wang, Q. Liu, Preparation and luminescence properties of sio2/$lu_2si_2o_7$:ce composite starting from mesopore template, RSC Adv. 4 (64) (2014) 33819–33825.
[50] D. Pauwels, N.L. Masson, B. Viana, A. Kahn-Harari, E.V.D. van Loef, P. Dorenbos, C.W.E. van Eijk, A novel inorganic scintillator: $Lu_2si_2o_7$:ce3+ (lps), IEEE Trans. Nucl. Sci. 47 (6) (2000) 1787–1790.
[51] C. Greskovich, S. Duclos, Ceramic scintillators, Annu. Rev. Mater. Sci. 27 (1997) 69–88.
[52] H. Feng, M.M.C. Chou, C.L. Chen, W.S. Xu, Z.S. Liu, G.H. Ren, Optical, scintillation and thermally stimulated luminescence properties of sc2si2o7:ce single crystal grown by floating zone method, Opt. Mater. 34 (7) (2012) 1003–1006.
[53] D. Napierska, L.C. Thomassen, V. Rabolli, D. Lison, L. Gonzalez, M. Kirsch-Volders, J.A. Martens, P.H. Hoet, Size-dependent cytotoxicity of monodisperse silica nanoparticles in human endothelial cells, Small 5 (7) (2009) 846–853.